Accepted Manuscript

$CaCO_3$ nanoparticles as an ultra-sensitive tumor-pH-responsive nanoplatform enabling real-time drug release monitoring and cancer combination therapy

Ziliang Dong, Liangzhu Feng, Wenwen Zhu, Xiaoqi Sun, Min Gao, He Zhao, Yu Chao, Zhuang Liu

PII: S0142-9612(16)30523-3

DOI: 10.1016/j.biomaterials.2016.09.025

Reference: JBMT 17727

To appear in: *Biomaterials*

Received Date: 25 July 2016

Revised Date: 26 September 2016

Accepted Date: 29 September 2016

Please cite this article as: Dong Z, Feng L, Zhu W, Sun X, Gao M, Zhao H, Chao Y, Liu Z, $CaCO_3$ nanoparticles as an ultra-sensitive tumor-pH-responsive nanoplatform enabling real-time drug release monitoring and cancer combination therapy, *Biomaterials* (2016), doi: 10.1016/j.biomaterials.2016.09.025.

$CaCO_3$ Nanoparticles as an Ultra-sensitive Tumor-pH-Responsive Nanoplatform Enabling Real-Time Drug Release Monitoring and Cancer Combination Therapy

Ziliang Dong[1], Liangzhu Feng[1]*, Wenwen Zhu[1], Xiaoqi Sun[1], Min Gao[1], He Zhao[2], Yu Chao[1], Zhuang Liu[1]*

1. Institute of Functional Nano & Soft Materials (FUNSOM), Jiangsu Key Laboratory for Carbon-Based Functional Materials & Devices, Soochow University, 199 Ren'ai Road, Suzhou, 215123, Jiangsu, PR China.

2. Department of Radiology, Children's Hospital of Soochow University, Suzhou 215003, Jiangsu, PR China.

*E-mail: zliu@suda.edu.cn; liangzhu.f@gmail.com

Abstract

The exploration of stimuli-responsive nano-theranostics provides powerful tools for simultaneously enhancing the accuracy and efficiency of cancer therapies. Herein, we develop mono-dispersed $CaCO_3$ nanoparticles modified with polyethylene glycol (PEG) as a multifunctional nano-carrier for efficient loading of both Mn^{2+}-chelated chlorin e6 (Ce6(Mn)) as a photosensitizer, and doxorubicin (DOX) as a chemotherapy drug. Our $CaCO_3$@Ce6(Mn)-PEG(DOX) nanoparticles, while being stable under physiological pH at 7.4, appear to be highly sensitive to reduced pH and would be rapidly degraded under slightly acidic environment, effectively releasing loaded therapeutic agents. Interestingly, owing to released Ce6(Mn), those nanoparticles show an interesting pH-dependent T1 signal enhancement under magnetic resonance (MR) imaging, which could be utilized for real-time monitoring of drug release. As discovered by MR and fluorescence imaging, intravenously (i.v.) injected $CaCO_3$@Ce6(Mn)/DOX-PEG could gradually accumulate in the tumor, contributing to a superior synergistic anti-tumor effect in the combined photodynamic & chemotherapy. In conclusion, we have developed a tumor-pH-activated nanocarrier based on biodegradable $CaCO_3$ nanoparticles, which may be an ideal cancer theranostic nanoplatform with substantial potential for future clinical translation.

Introduction

The unknown effective drug dose, that is the amount of therapeutic agents reaching diseased regions such as tumors in their activated form, for each individual patient is an important uncertainty towards accurate medicine, and often leads to over-dosing or insufficient dosing during treatment. To this end, the development of stimuli-responsive theranostic nano-platforms by integrating imaging and therapeutic functions has received a great deal of attention in recent years [1-3]. On one hand, imaging is able to guide the planning of therapies, particularly for those employing external stimuli (e.g. radiotherapy [4, 5], phototherapy[6-8], etc.), so as to selectively and efficiently destroy tumors while sparing normal tissues [9-11]. On the other hand, by visual imaging monitoring, the drug release profile inside the tumor in response to external or internal stimuli may also be monitored in the real time, facilitating the optimization of therapeutic doses and treatment time-windows[12-15]. Therefore, developing biocompatible / biodegradable smart theranostic nano-platforms to realize imaging-monitored therapy has become an attractive direction in the areas of nanomedicine and cancer therapy.

Over the past decade, the emergence of calcium-based biomineralized nanomaterials, such as calcium carbonate ($CaCO_3$) [16-18], calcium phosphate ($Ca(H_2PO_4)_2$), hydroxy apatite ($Ca_5(PO4)_3OH$) and tri-calcium phosphate ($Ca_3(PO4)_2$) [19, 20], has brought new opportunities to build theranostic nano-platforms owing to the excellent biocompatibility and biodegradability of those materials. In particular, nanoscale $CaCO_3$ which is stable under neutral pH and would be decomposed into Ca^{2+} and CO_2 under acidic pH has been proposed as pH-responsive drug delivery systems for delivery of chemotherapeutics or nucleic acids[21-24]. For example, Zhao et al. presented a mild approach to prepare porous $CaCO_3$ nanospheres, which after loading with doxorubicin (DOX) exhibited greatly enhanced therapeutic effects over the free drug towards tumor cells [25]. In another work, Su and co-workers designed an efficient method to produce well-dispersed polyacrylic acid/$CaCO_3$ nanoparticles with high DOX loading for in vivo liver cancer chemotherapy [23]. In a more recent work, Achilefu et al. prepared monodispersed $CaCO_3$ nanoparticles and found them to be capable of modulating the tumor acidic environment to offer potential therapeutic benefits [26]. Despite those unique features of nanoscale $CaCO_3$ nanoparticles as drug delivery systems, their applications as smart stimulus-responsive theranostic platforms by integrating imaging agents and therapeutic functions for precise disease treatment at the in vivo

level has been rarely reported to our best knowledge.

In this work, we develop mono-dispersed polyethylene glycol (PEG)-modified $CaCO_3$ nanoparticles with excellent colloidal stability. In such nanoparticles, Mn^{2+}-chelated chlorin e6 (Ce6(Mn)), a photosensitizer for photodynamic therapy [27], is loaded into nanoscale $CaCO_3$ by co-precipitation during the formulation of $CaCO_3$ nanoparticles. Interestingly, the as-synthesized Ce6(Mn)@$CaCO_3$–PEG nanoparticles appear to be highly sensitive to pH and would be rapidly degraded under slightly acidic solutions, leading to efficient release of Ce6(Mn) and thereby significantly enhanced T1-contrast under magnetic resonance (MR) imaging (with the r1 value increased by one order of magnitude to 11.48 $mM^{-1}s^{-1}$). Additionally, the mesoporous structure of Ce6(Mn)@$CaCO_3$–PEG could enable efficient loading of chemotherapeutic agent, doxorubicin (DOX), whose release is also pH dependent and shows positive correlation with T1-signal enhancement under MR imaging, allowing real-time monitoring of drug release. Importantly, utilizing such multifunctional biodegradable nanoparticles, we realize a synergistic photodynamic & chemotherapy of cancer in vivo under a precise multimodal-imaging guidance by MR and fluorescence imaging [28]. Thus, our results highlight $CaCO_3$ nanoparticles with great biocompatibility and biodegradability as a smart tumor-pH-responsive drug delivery platform useful for applications in cancer theranostics.

Experimental section

Materials: Calcium chloride dihydrade ($CaCl_2{\cdot}2H_2O$) and ammonia bicarbonate (NH_4HCO_3) were purchased from Sinopharm Chemical Reagent CO, Ltd., China. Doxorubicin (DOX) was bought from Beijing Hua Feng United Technology Co. Ltd. Cholesterol, manganese chloride ($MnCl_2$) and Chlorine e6 (Ce6) ware from J&K Chemical Co. 1, 2-dioleoyl-sn-glycero-3-phosphate (sodium salt) (DOPA), and 1,2-distearoyl-sn-glycero-3-phosphoethanolamine-N-(methoxy(polyethylene glycol)-5000) DSPE-PEG5k was purchased from Avanti. 1, 2-dihexadecanoyl-sn-glycero-3-phosphocholine (DPPC) was purchased from xi'an ruixi biological technology Co., Ltd. Fetal bovine serum (FBS) and Trypsin-EDTA were purchased from Invitrogen (USA). RPMI 1640 medium was purchased from Nanjing Key Gen Biotech. Co., Ltd., China. All aqueous solutions used in experiment were prepared by using deionized water (18.2 MΩ.cm) obtained from Milli-Q water purification system.

Synthesis of porous Ce6(Mn)@$CaCO_3$ nanoparticles

Ce6(Mn)@$CaCO_3$ particles were synthesized by a gas diffusion reaction. Briefly, 150 mg $CaCl_2 \cdot H_2O$, 10 mg Ce6 (pre-dissolved in DMSO) and 3 mg $MnCl_2$ were dissolved in 100 mL ethanol in a glass bottle covered by an aluminum foil which was punctured with several pores. Then, the bottle was put into a vacuum drying chamber containing 5 g dry ammonia bicarbonate (NH_4HCO_3). After keeping the whole system in a vacuum environment for 24 h, Ce6(Mn)-loaded $CaCO_3$ nanoparticles were obtained and could be separated by centrifugation at 8000 rpm. Those nanoparticles were re-dispersed in anhydrous ethanol for further modification.

PEGylation of Ce6(Mn)@$CaCO_3$ nanoparticles

A two-step approach was conducted to modify the above nanoparticles. Firstly, 20 mg Ce6(Mn)@$CaCO_3$ in ethanol solution and 1 ml DOPA solution (2 mg/ml in chloroform) was mixed under ultrasonication for 20 min. The obtained turbid solution was centrifuged to remove unbounded free DOPA and redispersed in chloroform. PEGylation of nanoparticles was then conducted by mixing a chloroform solution of DPPC, cholesterol and DSPE-PEG at the 4:4:2 molar ratio with Ce6(Mn)@$CaCO_3$-DOPA under vigorously stirring overnight. Afterwards, chloroform was evaporated and the obtained Ce6(Mn)@$CaCO_3$-PEG nanoparticles were dissolved in aqueous solution for further use.

Characterization

The transmission electron microscopy (TEM) images including bright field (BF) and high angle annular dark field (HAADF) images of the Ce6(Mn)@$CaCO_3$ nanoparticles were taken by using a FEI Tecnai F20 transmission electron microscope at an acceleration voltage of 200 kV (FEI company). Scanning Electron Microscopy (SEM) images were taken by a FEI Quanta 200F scanning electron microscope. UV-Vis-NIR spectra were acquired by using a PerkinElmer Lambda 750 UV-Vis-NIR spectrophotometer. Dynamic light scattering (DLS) measurement was conducted on ZEN3690 zetasizer (Malvern, USA). Nitrogen sorption studies by the Brunauer-Emmett-Teller (BET) method were performed with Micromeritics ASAP 2020 HD88.

Doxorubicin loading

Ce6(Mn)@$CaCO_3$-PEG was firstly mixed with different concentrations of DOX in phosphate buffer at pH 8.0 (20 mM). After stirring in dark for 24 h, DOX loaded Ce6(Mn)@$CaCO_3$-PEG nanoparticles were collected by the ultra-filtration filters (Millipore, MWCO = 100 kDa) to remove unloaded DOX. The DOX loading capacity was detected by UV-Vis-NIR spectra with absorption peak at 490 nm.

In vitro drug release

Ce6(Mn)@$CaCO_3$-PEG(DOX) was dissolved in phosphate buffered saline (PBS) at different pH values (pH=5.5, 6.5 and 7.4) under 37 ^{o}C. At different time points, the solutions were centrifuged to collect the supernatants. The released DOX in the supernatant was measured by UV-Vis-NIR spectra. The releasing behavior of Ce(Mn) was also conducted by measuring the Ce6 characteristic peak with UV-Vis-NIR spectra.

pH-dependent singlet oxygen generation (SOG) measurement

The SOG measurement was based on the protocol reported previously[29]. In brief, 10 μl SOSG (0.5 mM in methanol) was mixed with 1990 μl free Ce6 or Ce6(Mn)@$CaCO_3$-PEG(DOX) at different pH values (pH=5.5, 6.8 and 7.4) ([Ce6]=1μl). The SOG of different samples was induced by irradiation with a 660 nm LED light source at a power density of 5 mW/cm^2 for different time periods (0 min, 10 min, 20 min, 30 min, 40 min and 50 min). The fluorescence intensity of SOSG was detected (λex = 494 nm) after irradiation.

In vitro pH-sensitive MR imaging

For in vitro MR imaging, nanoparticles in PBS at three pH values (pH=5.5, 6.5 and 7.4) with a series of Mn^{2+} concentrations were scanned by a 3 T clinical MRI scanner (BrukerBiospin Corporation, Billerica, MA, USA).

Cellular experiments

4T1 cells were purchased from American Type Culture Collection (ATCC) and cultured under standard conditions (37 ^{o}C, 5% CO_2). Firstly, for confocal imaging, 4T1 cells were seeded in 35 mm

culture dishes and treated with Ce6(Mn)@$CaCO_3$-PEG(DOX) or free Ce6 with the same Ce6 concentration for 4 h. After washing with PBS (pH= 7.4) for several times, the cells were labeled with 4, 6-diamino-2-phenylindole (DAPI) and then imaged by a confocal fluorescence microscope (Leica SP5II laser scanning confocal microscope).

To test the chemotherapy efficacy of DOX loaded particles, 4T1 cells were seeded in 96-well plates with 1 x 10^4 cells / well and incubated until adherent. Then, various concentrations of Ce6(Mn)@$CaCO_3$-PEG(DOX) or free DOX were added and incubated with cells for another 24 h. Afterwards, the cells were washed with free cell culture medium for several times and then a standard MTT assay was carried out to determined the relative cell viabilities.

To test the PDT effect, 4T1 cells seeded in 96-well plates were incubated with various concentrations of Ce6(Mn)@$CaCO_3$-PEG and free Ce6. After 4 h of incubation, the samples were irradiated by 660-nm light at a power density of 5 mW/cm^2 for 0.5 h. Afterwards the cells were incubated for another 24 h. Then, the standard MTT assay was carried out to determine the relative cell viabilities.

For in vitro combination therapy, 4T1 cells in 96 wells plate were incubated with various concentrations of Ce6(Mn)@$CaCO_3$-PEG or Ce6(Mn)@$CaCO_3$-PEG(DOX). After 4 h of incubation, the cells were irradiated by 660-nm light at a power density of 5 mW/cm^2 for 0.5 h. After another 24 h of incubation, the MTT assay was carried out to determine the relative cell viabilities compared with the untreated group.

Mouse tumor model

In our experiments, female Balb/c mice were purchased from Nanjing Peng Sheng Biological Technology Co, Ltd. Animal experiments were performed following protocols approved by Soochow University Laboratory Animal Center. To develop the tumor model, 1 x 10^6 4T1 cells suspended in 50 μL PBS were subcutaneously injected into the back of each mouse. After about one week, the average tumor sizes would reach to about 60 mm^3.

In vivo imaging

For in vivo fluorescence imaging, 200 μL of Ce6(Mn)@$CaCO_3$-PEG(DOX) ([Ce6]=0.45 mg/ml) was intravenously injected into each mouse. Then, in vivo fluorescence imaging at different

time points (1 h, 2 h, 4 h, 8 h, 12 h and 24 h) was carried out using a Maestro EX in vivo optical imaging system (Cambridge Research and Instrumentation, Inc.). The autofluorescence background was removed by the spectrum unmixing software. The mice were sacrificed after 24 h of injection, with and their major organs (liver, spleen, kidney, heart, lung and tumor) collected for ex vivo imaging. The in vivo T1-weighted MR animal imaging was performed under a 3-T clinical MR scanner with a special coil designed for small-animal imaging.

In vivo combination therapy

For in vivo combination therapy, 4T1 tumor-bearing mice were divided into five groups (n=5 each group): (1) PBS, (2) Free Ce6 + Free DOX (with 660-nm light exposure), (3) Ce6(Mn)@$CaCO_3$-PEG(DOX), (4) Ce6(Mn)@$CaCO_3$-PEG (with 660-nm light exposure) and (5) Ce6(Mn)@$CaCO_3$-PEG(DOX) (with 660-nm light exposure). In each group, 200 μL of agent with the same Ce6 or DOX equivalent concentration (dose: DOX: 5 mg/kg, Ce6 4.5 mg/kg) were intravenously injected into each mouse. After 24 h of injection, the mice were irradiated by 660-nm light at a power density of 5 mW/cm^2 for 1 h. After treatment, the tumor sizes were monitored by a digital caliper to record the lengths and widths every two days. The tumor volumes were calculated by "volume = length x $width^2/2$".

Result and discussion

The fabrication of photosensitizer Ce6 loaded $CaCO_3$ nanoparticles and the subsequently modification with PEG is illustrated in **Figure 1a**. Nano-sized amorphous $CaCO_3$ nanoparticles were firstly synthesized by a gas diffusion reaction according to the literature report [30] with some modifications. Mn^{2+}-chelated Ce6 (Ce6(Mn)) was prepared by simply mixing Ce6 and $MnCl_2$ at the 1:1 molar ratio to allow the chelation of Mn^{2+} at the center of the porphyrin structure in Ce6 [31, 32]. In the process of $CaCO_3$ growth, such Ce6(Mn) was pre-added in the $CaCl_2$ solution, into which NH_3 decomposed from NH_4HCO_3 was slowly dissolved. As shown under SEM (**Figure 1b)** and TEM (**Figure 1c**), as-synthesized Ce6(Mn)@$CaCO_3$ nanoparticles were monodispersed with an average diameter of around 100 nm. The surface area and the average size of those nanoparticles were measured by BET to be 200 $m^2\ g^{-1}$ and 3.5 nm, respectively (**Figure S1, Supporting information**), indicating their mesoporous structure which may be helpful for the subsequent drug

loading and controllable release. The strong Ce6-characteristic absorption peaks appeared at 404 nm and 660 nm in the UV-VIS-NIR spectrum of our obtained Ce6(Mn)@$CaCO_3$ nanoparticles (**Figure 1e**), suggesting the successful encapsulation of Ce6 within those nanoparticles, likely owing to the strong interaction between carboxyl groups in Ce6 and Ca^{2+} ions. An elemental mapping in the high-angle annular dark fields scanning TEM (HAADF–STEM) image (**Figure 1d**) further illustrated the homogenous distribution of Mn element in those Ce6(Mn)@$CaCO_3$ composite nanoparticles.

Next, PEGylation was conducted to modify those as-made Ce6(Mn)@$CaCO_3$ nanoparticles by a two-step approach to improve their water solubility and colloidal stability. Firstly, hydrophobic DOPA-coated Ce6(Mn)@$CaCO_3$ nanoparticles were prepared by mixing DOPA and Ce6(Mn)@$CaCO_3$ under ultrasonication. The coordination of Ca^{2+} on the surface of $CaCO_3$ nanoparticles with the phosphate group in DOPA would allow stable anchoring of hydrophobic aliphatic chains onto those nanoparticles, offering them highly lipophilic surfaces. Subsequent PEGylation was performed by mixing a chloroform solution of cholesterol, DPPC and DSPE-PEG_{5000} at a 4:4:2 molar ratio [33] with Ce6(Mn)@$CaCO_3$-DOPA under stirring overnight. After evaporating the chloroform solvent, a lipid bilayer would form on the nanoparticle surface, obtaining Ce6(Mn)@$CaCO_3$-PEG nanoparticles with great water solubility (**Figure S2, Supporting information**). The dynamic light scattering (DLS) data showed the hydrodynamic size of Ce6(Mn)@$CaCO_3$-PEG to be around ~150 nm in the aqueous solution (**Figure 1f**). Besides, those PEGylated nanoparticles exhibited excellent dispersibility in water, phosphate buffered saline (PBS) and cell medium without any precipitation (**Figure 1g**), allowing their further applications in biological systems.

It is known that $CaCO_3$ can be dissolved in the acidic media into Ca^{2+} and CO_2. We thus tested the pH sensitivity of our Ce6(Mn)@$CaCO_3$-PEG nanoparticles by immersing them in buffers with various pH values (5.5, 6.5 and 7.4). TEM imaging was conducted to observe the morphology of those particles at different time points (**Figure 2b**). Our Ce6(Mn)@$CaCO_3$-PEG nanoparticles appeared to be quite stable under pH 7.4 without showing any notable change in their sizes and structures. In contrast, within a mild acidic buffer at pH 6.5, those Ce6(Mn)@$CaCO_3$-PEG nanoparticles were gradually dissociated and largely lost their sphere morphology after 2 hours. More amazingly, we observed that Ce6(Mn)@$CaCO_3$-PEG nanoparticles under pH 5.5 would be

rapidly decomposed, leaving no visible particle structure under TEM within as short as 5 min, indicating the ultra-sensitive pH responsibility of such Ce6(Mn)@$CaCO_3$-PEG nanoparticles. Meanwhile, the time-dependent changes of hydrodynamic sizes of those nanoparticles under different pH values were monitored by DLS. As shown in **Figure 2c**, at pH 6.5, our nanoparticles would be slowly dissociated, presenting a time-dependent decrease in particle sizes. Amazingly, the process of dissociation was dramatically accelerated at pH 5.5. In contrast, the hydrodynamic sizes of Ce6(Mn)@$CaCO_3$-PEG nanoparticles dispersed under neutral pH 7.4 showed no obvious change, consistent to the TEM observation. Particularly worth mentioning is that the property of acid-triggered structure transformation could be suitable for long and stable blood circulation under the physiological pH, as well as quick cargo release within the tumor microenvironment with reduced pH.

Based on the fact that the spin-lattice (r1) proton relaxivity is proportional to the number of water molecules that coordinates with unpaired electrons in the MR contrast agent, we then investigated whether the pH-responsive dissociation of Ce6(Mn)@$CaCO_3$-PEG nanoparticles would lead to pH-dependent release of Ce6(Mn) and thereby enhanced T1-contrast under MR imaging **(Figure 2a)** [34]. Firstly, we measured the release profiles of Ce6(Mn) under different pH values (**Figure 3a**) based on the characteristic absorbance peak of Ce6. Consistent with the pH-dependent decomposition behaviors of $CaCO_3$ nanoparticles, the release of Ce(Mn) from Ce6(Mn)@$CaCO_3$-PEG appeared to be ultra-fast under pH 5.5, and obviously slower under increased pHs. Correspondingly, under T1-weighted MR imaging (**Figure 3b**), obvious concentration-dependent brightening effects could be observed for Ce6(Mn)@$CaCO_3$-PEG incubated at different pH values for 4 h. Interestingly, the longitudinal relaxation (r1) dramatically increased from 1.156 mM^{-1} s^{-1} at pH 7.4 to 11.48 mM^{-1} s^{-1} at pH 5.5, by nearly one order of magnitude (**Figure 3c, Figure S3, Supporting information**). In contrast, free Ce6@Mn showed no significant change in its MR contrasting ability at the variation of pH values (**Figure S4a-b, Supporting information**). Considering the weak acidic environment inside solid tumors, our Mn^{2+} encapsulated nano-agents would offer a powerful tool benefited from its pH-responsive longitudinal relaxivity for the noninvasive detection of tumors distinguished from normal tissues.

Next, we measured the light-triggered production of $^1O_2$ from Ce6(Mn)@$CaCO_3$-PEG by singlet oxygen sensor green (SOSG), a SO specific dye, under the irradiation of 660-nm light. As

shown in **Figure S5, Supporting information**, the efficiency of SO production from Ce6(Mn)@$CaCO_3$-PEG determined by the recovered SOSG fluorescence was found to be pH dependent. For Ce6(Mn)@$CaCO_3$-PEG nanoparticles under pH 7.4, the light-triggered SO generation appeared to be less efficient compared to that of free Ce6(Mn). In contrast, owing to the dissociation of nanoparticles under acid condition at pH 5.5, more efficient $^1O_2$ generation from the Ce6(Mn)@$CaCO_3$-PEG sample was observed, reaching to a level similar to that of free Ce6(Mn). This pH-activated photosensitizing performance could be valuable for tumor-specific photodynamic cancer treatment owing to the unique acidic tumor microenvironment.

As mentioned above, Ce6(Mn)@$CaCO_3$-PEG nanoparticles exhibited mesoporous structure, which could be suitable for drug loading. Doxorubicin (DOX), a commonly used chemotherapy drug, was chosen as the model drug. By mixing Ce6(Mn)@$CaCO_3$-PEG with DOX solutions at different concentrations under pH 8.0 overnight and then washing to remove free DOX, a DOX-characteristic absorption peak at 490 nm appeared in the obtained nanoparticles (**Figure 3d**), suggesting the successful DOX loading into Ce6(Mn)@$CaCO_3$-PEG. Besides, the drug loading efficiency on Ce6(Mn)@$CaCO_3$-PEG(DOX) increased with the increasing amounts of feeding DOX, showing a saturated loading capacity to be as high as 22 % (with a loading efficiency of ~11% at this condition). (**Figure S6, Supporting information**).

Owing to the pH-dependent decomposition of $CaCO_3$ nanoparticles, we would thus expect a pH-responsive DOX release behavior, which in turn may be real-time monitored by T1-weighted MR imaging. The DOX release from Ce6(Mn)@$CaCO_3$-PEG(DOX) under various pH values (5.5, 6.5, 7.4) was then measured (**Figure S7, Supporting information**). As expected, the release of DOX was obviously pH-dependent, presenting a similar tendency to that of Ce6(Mn). To figure out the correlation between the percentage of DOX release and the T1-MR signal enhancement, we further recorded the MR signal changes under different pH values over time. As shown in **Figure 3e**, an obvious pH-dependent brightening effect could be observed. Beside, by recording the MR intensity enhancement, we then built the correlation between the time-dependent DOX release and enhanced MR intensities (**Figure 3f**). Excitingly, great correlations were presented at all three pH values, indicating that MR imaging could be utilized for real time monitoring of DOX release from Ce6(Mn)@$CaCO_3$-PEG(DOX) based on the enhanced T1 MR signals.

Based on this multifunctional nanoplatform, next, we studied the interactions of

Ce6(Mn)@$CaCO_3$-PEG(DOX) nanoparticles in vitro with cells. To study cellular uptake ability of our nanoparticles, 4T1 murine breast cancer cells were incubated with Ce6(Mn)@$CaCO_3$-PEG(DOX) for 4 h at 37 ^oC, and then imaged by a fluorescence laser scanning confocal microscope. As shown in **Figure 4a**, strong Ce6 and DOX fluorescence signals emerged inside cells after incubation with Ce6(Mn)@$CaCO_3$-PEG(DOX), suggesting the efficient cellular uptake of our nanoparticles. Notably, while Ce6 fluorescence was found mostly in cytoplasm, strong DOX fluorescence appeared inside cell nuclei, indicating the dissociation of Ce6(Mn)@$CaCO_3$-PEG(DOX) nanoparticles inside cells (e.g. inside cell lysosomes with reduced pH).

We then evaluated the cell killing efficacy by single chemo- or photodynamic therapy. Firstly, 4T1 cells were incubated with free DOX or Ce6(Mn)@$CaCO_3$-PEG(DOX) at the equivalent DOX concentrations. After 24 h. the relative cell viabilities were determined by the methylthiazolyltetrazolium (MTT) assay (**Figure 4b**). Ce6(Mn)@$CaCO_3$-PEG(DOX) showed a comparable cell toxicity to that of free DOX. For photodynamic therapy, 4T1 cells were incubated with various concentrations of Ce6(Mn)@$CaCO_3$-PEG or free Ce6 and then irradiated under 660-nm light (5 mM/cm^2) for 0.5 h. After further incubation for 24 h, the relative cell viabilities were also determined by the MTT assay (**Figure 4c**), which uncovered that the nanoparticle formulation of Ce6 showed similar photodynamic cell killing efficiency compared to its free form.

For in vitro combination chemo-& photodynamic cancer therapy, 4T1 cells were treated with different concentrations of the following agents: (1) Ce6(Mn)@$CaCO_3$-PEG, (2) Ce6(Mn)@$CaCO_3$-PEG (with 660-nm light exposure), (3) Ce6(Mn)@$CaCO_3$-PEG(DOX), (4) Ce6(Mn)@$CaCO_3$-PEG(DOX)(with 660-nm light exposure). After incubation for 4 h, the groups (2) and (4) were irradiated under 660-nm LED light (5 mM/cm^2) for 0.5 h. After further incubation for 24 h, the relative cell viabilities were determined by the MTT assay (**Figure 4d**). Ce6(Mn)@$CaCO_3$-PEG without light irradiation showed negligible cell toxicity, demonstrating the good biocompatibility of our nano-agents. Meanwhile, the combination of photodynamic & chemotherapy showed greatly improved cancer cell killing ability compared with any mono-therapy at the same respective nanoparticle concentrations.

The in vivo behaviors of Ce6(Mn)@$CaCO_3$-PEG(DOX) nanoparticles were then evaluated in animal model experiments. Firstly, Ce6(Mn)@$CaCO_3$-PEG(DOX) (dose: 4.5 mg/kg for Ce6) was

intravenously (i.v.) injected into each female Balb/c mouse (n=3) with blood extracted at certain time intervals. As shown in **Figure S8, Supporting information**, the Ce6 signals in blood samples declined over time following a two-compartment model, with the first (t1/2(α)) and second (t1/2(β)) phases of circulation half-lives determined to be 1.19 ± 0.84 and 14.15 ± 0.77 h, respectively. The long blood circulation is favorable for tumor passive targeting via the enhanced permeability and retention (EPR) effect.

Then, in vivo fluorescence imaging was performed after i.v. injection of Ce6(Mn)@$CaCO_3$-PEG(DOX) into mice bearing 4T1 murine breast tumors. At the different time points, the mice were imaged under the Maestro EX in vivo optical imaging system (CRi, Inc.) by recording the fluorescence of Ce6 (**Figure 5a**). Strong Ce6 fluorescence gradually showed up at the tumor site, suggesting the time-dependent increase in the tumor uptake of Ce6(Mn)@$CaCO_3$-PEG(DOX) nanoparticles by the EPR effect (**Figure S9, Supporting information**). At 24 h post injection of Ce6(Mn)@$CaCO_3$-PEG(DOX), those mice were sacrificed and their major organs together with tumors were collected for ex vivo imaging. As shown in **Figure 5b**, the tumor was the brightest among all other organs, suggesting the high tumor passive accumulation of those nanoparticles. To quantitatively analyze the biodistribution of Ce6(Mn)@$CaCO_3$-PEG(DOX), the organs were homogenized within a lysis buffer to obtain tissue lysates, which were diluted and measured by a fluoromter to determine the concentration of Ce6 in different organs (**Figure 5c**). Interestingly, at 24 h post i.v. injection of those nanoparticles, the tumor uptake reached as high as 25 percent-of-injected-dose-per-gram-tissue (%ID/g), which was even higher than that in reticuloendothelial system (RES) such as liver and spleen responsible for the clearance of exogenous nanoparticles [35]. Kidney is another organ with relatively high Ce6 signals, suggesting the possible in vivo degradation of Ce6(Mn)@$CaCO_3$-PEG(DOX) nanoparticles and then the excretion of Ce6(Mn) in its free form.

It has been widely accepted that multimodal tumor imaging by combining at least two kinds of imaging techniques could compensate for the shortcomings of a single imaging modality and may improve the accuracy of tumor diagnosis [36-40]. Therefore, in our system, apart from fluorescence imaging, in vivo T1-weighted MR imaging was also conducted for tumor-bearing mice after i.v. injection of Ce6(Mn)@$CaCO_3$-PEG(DOX) (**Figure 5d**). An obviously brightening effect could be found in the tumor region 24 h post injection. Meanwhile, through region-of-interest (ROI)

quantified analysis, the quantitative MR imaging showed as high as 8-fold of T1-signal enhancement, demonstrating the high tumor uptake efficiency of those nanoparticles (**Figure 5e**).

Next we would like to further demonstrate the possibility of in vivo drug release monitoring by MR imaging. Balb/c mice bearing murine breast cancer 4T1 tumors were used in our experiments. The equivalent amounts of Ce6(Mn)@$CaCO_3$-PEG(DOX) solutions were separately injected into the tumor and the muscle on two opposite sides of a same mouse. As expected, strong T1 MR signals appeared in the tumor after injection of those nanoparticles, and gradually increased over time within 2 h (**Figure 5f**). In contrast, the enhancement of T1 MR signals in the muscle with the same amount of Ce6(Mn)@$CaCO_3$-PEG(DOX) injected was found to be much less significant. The quantitative measurement was conducted by calculating Tumor : Muscle (T/M) T1-MR signal intensities at different time intervals post injection of Ce6(Mn)@$CaCO_3$-PEG(DOX) (**Figure 5g)**. Such a T/M ratio showed gradual enhancement over time and reached a rather high level (T/M = 2.32 ± 0.23) at 1 h post-treatment. Our in vivo MR imaging results evidenced that such Ce6(Mn)@$CaCO_3$-PEG(DOX) nanoparticles, while being stable inside normal tissues (pH 7.4), would be dissociated inside the tumor with reduced pH (6.0-6.6 for 4T1 tumors) [18], leading to the efficient release of loaded imaging and therapeutic molecules. Therefore, we would be able to use MR imaging to real-time monitor in vivo drug release inside the tumor, potentially meaningful for optimization of therapeutic doses and prediction of therapeutic outcomes [13, 41]. Our observation here also explains the dramatically enhanced T1-MR-signals in the tumor after i.v. injection of Ce6(Mn)@$CaCO_3$-PEG(DOX) nanoparticles (**Figure 5d&e**), which after entering tumors via blood circulation may gradually decompose inside the acidic tumor microenvironment.

Encouraged by the high tumor uptake of Ce6(Mn)@$CaCO_3$-PEG(DOX) after systemic administration, in vivo combined chemo-& photodynamic cancer treatment was then performed. Female Balb/c mice bearing 4T1 tumors were randomly divided into five groups for the following treatments: (1) PBS, (2) Free Ce6 + Free DOX (with 660-nm light exposure), (3) Ce6(Mn)@$CaCO_3$-PEG(DOX), (4) Ce6(Mn)@$CaCO_3$-PEG (with 660-nm light exposure) and (5) Ce6(Mn)@$CaCO_3$-PEG(DOX) (with 660-nm light exposure). All agents were i.v. injected into those mice (dose: Ce6=4.5 mg/kg, DOX=5 mg/kg). At 24 h post injection, the corresponding groups by PDT-treatment (group 2, 4, 5) were irradiated with 660-nm light at a power density of 5 mW/cm^2 for 1 h. Later, the tumor volumes and body weights were monitored every the other day (**Figure 6a**).

It was found that the tumor growth in group 2 (free DOX + free Ce6, with light exposure) was only slightly inhibited, likely owing to the inefficient tumor retention of those small molecules (DOX and Ce6). Tumors in Ce6(Mn)@$CaCO_3$-PEG(DOX) treated group (group 3) and Ce6(Mn)@$CaCO_3$-PEG (with light exposure) treated group (group 4) both showed moderately delayed growth in the first few days, but grew rapidly later on, indicating that the tumor growth could not be effectively inhibited by single chemotherapy or photodynamic treatment at the tested dsoes. Remarkably, the tumor growth on mice treated by Ce6(Mn)@$CaCO_3$-PEG(DOX) (with light exposure) was greatly inhibited after combined photodynamic & chemotherapy, demonstrating the superior synergistic antitumor effect by those two kinds of therapies. Moreover, the average body weights of different groups showed no significant variation (**Figure 6b**), indicating no obvious acute side effect to the treated mice. After treatment, the tumors in different groups were also harvested and photographed. As illustrated in **Figure 6c & d**, tumors treated by Ce6(Mn)@$CaCO_3$-PEG(DOX) (with 660-nm light exposure) were much smaller both in their weights and visible sizes, consistent to the above tumor growth curve data.

Afterwards, slices of tumors with hematoxylin and eosin (H&E) staining were examined to further verify the therapeutic effects after various treatments (**Figure 6e)**. As expected, a much higher level of tumor damage appeared in the combination therapy group (group 5), whereas the other four groups showed little or no damage on tumor cells, which exhibited normal membrane morphology and nuclear structures. Correspondingly, deoxynucleotidyl transferase-mediated dUTP nick end labeling (TUNEL) staining of tumor slices also uncovered the highest level of cell apoptosis for tumors after the combined photodynamic & chemotherapy treatment with Ce6(Mn)@$CaCO_3$-PEG(DOX). Furthermore, histological examination of H&E stained slices of major organs illustrated no appreciable organ damage in group 5 after our nanoparticle-based combination therapy compared to untreated mice (**Figure S10, Supporting information**).

The $CaCO_3$ nanoparticle-based theranostic platform developed here has a number of unique features potentially superior to many other previously developed theranostic nanoparticles. (1) Unlike many other inorganic nanostructures, $CaCO_3$ exhibits inherent biocompatibility and biodegradability without long-term safety concerns when used in vivo. (2) Such $CaCO_3$ nanoparticles are ultra-sensitive to pH, effectively releasing therapeutic and imaging payloads under slightly acidic tumor pH. (3) The capability of using MR imaging to in vivo real-time monitor drug

release within our system would have great potential for future precision medicine, to facilitate the treatment planning and therapeutic response prediction. (4) The excellent therapeutic effect realized by our tumor pH-responsive combination therapy further promises future clinical translation of our nanoparticles in cancer theranostics.

Conclusion

In summary, we have successfully developed a new class of stimuli-responsive nanoplatform based on mono-dispersed PEG-modified $CaCO_3$ nanoparticles, which then are exploited as a multifunctional nano-carrier for efficient loading of different types of therapeutic and imaging molecules. While being stable under physiological pH at 7.4, our $CaCO_3$@Ce6(Mn)-PEG(DOX) nanoparticles would be rapidly degraded under slightly acidic solutions, leading to efficient release of both Ce6(Mn) and DOX, the former of which would result in significantly enhanced T1-contrast under MR imaging (with the r1 value increased by one order of magnitude at pH 5.5). Efficient tumor uptake of those nanoparticles is then revealed by in vivo multimodal imaging after systemic injection of $CaCO_3$@Ce6(Mn)-PEG(DOX). Moreover, utilizing such multifunctional biodegradable nanoparticles, we are able to realize a superior synergistic anti-tumor effect by combined photodynamic & chemotherapy. Therefore, this work presents a tumor-pH-activated nanocarrier based on $CaCO_3$ nanoparticles for imaging-monitored cancer therapy. Considering the inherent biocompatibility and biodegradability of $CaCO_3$, as well as its ultra-sensitive response to tumoral pH, $CaCO_3$ nanoparticles may indeed be a promising type of smart drug delivery nano-platform with significant potential in clinical translation.

Acknowledgments

We acknowledge the National 973 Programs of China (2012CB932600), the National Natural Science Foundation of China (51525203, 51222203), Collaborative Innovation Center of Suzhou Nano Science & Technology, the Priority Academic Program Development (PAPD) of Jiangsu Higher Education Institutions.

Reference

[1] Mura S, Nicolas J, Couvreur P. Stimuli-responsive nanocarriers for drug delivery. Nat. Mater. 2013;12:991-1003.

[2] Nguyen KT, Zhao Y. Engineered Hybrid Nanoparticles for On-Demand Diagnostics and Therapeutics. Acc. Chem. Res. 2015;48:3016-25.

[3] Wang S, Huang P, Chen X. Stimuli-Responsive Programmed Specific Targeting in Nanomedicine. ACS nano. 2016;10:2991-4.

[4] Locke JA, Dal Pra A, Supiot S, Warde P, Bristow RG. Synergistic action of image-guided radiotherapy and androgen deprivation therapy. Nat. Rev. Urol. 2015;12:193-204.

[5] Zhong X, Yang K, Dong Z, Yi X, Wang Y, Ge C, et al. Polydopamine as a Biocompatible Multifunctional Nanocarrier for Combined Radioisotope Therapy and Chemotherapy of Cancer. Adv. Funct. Mater. 2015;25:7327-36.

[6] Yatvin MB, Weinstein JN, Dennis WH, Blumenthal R. Design of liposomes for enhanced local release of drugs by hyperthermia. Science. 1978;202:1290-3.

[7] Cheng L, Wang C, Feng L, Yang K, Liu Z. Functional nanomaterials for phototherapies of cancer. Chem. Rev. 2014;114:10869-939.

[8] Yan H, Teh C, Sreejith S, Zhu L, Kwok A, Fang W, et al. Functional Mesoporous Silica Nanoparticles for Photothermal-Controlled Drug Delivery In Vivo. Angew. Chem. In. Ed. 2012;51:8373-7.

[9] Gross S, Gilead A, Scherz A, Neeman M, Salomon Y. Monitoring photodynamic therapy of solid tumors online by BOLD-contrast MRI. Nat. Med. 2003;9:1327-31.

[10] Grossi M, Morgunova M, Cheung S, Scholz D, Conroy E, Terrile M, et al. Lysosome triggered near-infrared fluorescence imaging of cellular trafficking processes in real time. Nat. Commun. 2016;7:10855.

[11] Kaittanis C, Shaffer TM, Ogirala A, Santra S, Perez JM, Chiosis G, et al. Environment-responsive nanophores for therapy and treatment monitoring via molecular MRI quenching. Nat. Commun. 2014;5:3384.

[12] Fan Z, Sun L, Huang Y, Wang Y, Zhang M. Bioinspired fluorescent dipeptide nanoparticles for targeted cancer cell imaging and real-time monitoring of drug release. Nat. Nano. 2016;11:388-94.

[13] Liu J, Bu J, Bu W, Zhang S, Pan L, Fan W, et al. Real-time in vivo quantitative monitoring of drug release by dual-mode magnetic resonance and upconverted luminescence imaging. Angew. Chem. In. Ed. 2014;53:4551-5.

[14] Yang K, Feng L, Liu Z. Stimuli responsive drug delivery systems based on nano-graphene for cancer therapy. Adv. Drug Deliv. Rev. 2016.

[15] null BL. A novel upconversion nanotheranostic agent for multi-modality imaging-guided chemotherapy with on-demand drug release. Sci. China Chem. 2015;58:970.

[16] Morse JW, Arvidson RS, Lüttge A. Calcium carbonate formation and dissolution. Chem. Rev. 2007;107:342-81.

[17] Maleki Dizaj S, Barzegar-Jalali M, Zarrintan MH, Adibkia K, Lotfipour F. Calcium carbonate nanoparticles as cancer drug delivery system. Expert Opin. Drug

Deliv. 2015;12:1649-60.
[18] Min KH, Min HS, Lee HJ, Park DJ, Yhee JY, Kim K, et al. pH-Controlled Gas-Generating Mineralized Nanoparticles: A Theranostic Agent for Ultrasound Imaging and Therapy of Cancers. ACS Nano. 2015;9:134-45.
[19] Baglioni P, Fiorentino S. Functional calcium phosphate composites in nanomedicine. 2016.
[20] Mi P, Kokuryo D, Cabral H, Wu H, Terada Y, Saga T, et al. A pH-activatable nanoparticle with signal-amplification capabilities for non-invasive imaging of tumour malignancy. Nat. Nanotech. 2016.
[21] Zhao Y, Luo Z, Li M, Qu Q, Ma X, Yu SH, et al. A preloaded amorphous calcium carbonate/doxorubicin@silica nanoreactor for pH-responsive delivery of an anticancer drug. Angew. Chem. In. Ed. 2015;54:919-22.
[22] Wang C-Q, Gong M-Q, Wu J-L, Zhuo R-X, Cheng S-X. Dual-functionalized calcium carbonate based gene delivery system for efficient gene delivery. RSC Adv. 2014;4:38623-9.
[23] Shi H, Li L, Zhang L, Wang T, Wang C, Zhu D, et al. Designed preparation of polyacrylic acid/calcium carbonate nanoparticles with high doxorubicin payload for liver cancer chemotherapy. CrystEngComm. 2015;17:4768-73.
[24] Chen S, Zhao D, Li F, Zhuo R-X, Cheng S-X. Co-delivery of genes and drugs with nanostructured calcium carbonate for cancer therapy. RSC Adv. 2012;2:1820-6.
[25] Zhao Y, Lin L-N, Lu Y, Chen S-F, Dong L, Yu S-H. Templating Synthesis of Preloaded Doxorubicin in Hollow Mesoporous Silica Nanospheres for Biomedical Applications. Adv. Mater. 2010;22:5255-9.
[26] Som A, Raliya R, Tian L, Akers W, Ippolito JE, Singamaneni S, et al. Monodispersed calcium carbonate nanoparticles modulate local pH and inhibit tumor growth in vivo. Nanoscale. 2016.
[27] Fan H, Yan G, Zhao Z, Hu X, Zhang W, Liu H, et al. A Smart Photosensitizer–Manganese Dioxide Nanosystem for Enhanced Photodynamic Therapy by Reducing Glutathione Levels in Cancer Cells. Angew. Chem. In. Ed. 2016;128:5567-72.
[28] Frangioni JV. In vivo near-infrared fluorescence imaging. Curr. Opin. Chem. Biol. 2003;7:626-34.
[29] Zhu W, Dong Z, Fu T, Liu J, Chen Q, Li Y, et al. Modulation of Hypoxia in Solid Tumor Microenvironment with MnO2 Nanoparticles to Enhance Photodynamic Therapy. Adv. Funct. Mater. 2016.
[30] Zhao Y, Lin LN, Lu Y, Chen SF, Dong L, Yu SH. Templating synthesis of preloaded Doxorubicin in hollow mesoporous silica nanospheres for biomedical applications. Adv. Mater. 2010;22:5255-9.
[31] Gong H, Dong Z, Liu Y, Yin S, Cheng L, Xi W, et al. Engineering of Multifunctional Nano-Micelles for Combined Photothermal and Photodynamic Therapy Under the Guidance of Multimodal Imaging. Adv. Funct. Mater. 2014;24:6492-502.
[32] Lovell JF, Jin CS, Huynh E, Jin H, Kim C, Rubinstein JL, et al. Porphysome nanovesicles generated by porphyrin bilayers for use as multimodal biophotonic

contrast agents. Nat. Mater. 2011;10:324-32.
[33] Liu D, Poon C, Lu K, He C, Lin W. Self-assembled nanoscale coordination polymers with trigger release properties for effective anticancer therapy. Nat. Commun. 2014;5:4182.
[34] Edelman RR, Warach S. Magnetic Resonance Imaging. N. Engl. J. Med. 1993;328:708-16.
[35] Phillips S, Escobar MR. The Reticuloendothelial System: A Comprehensive Treatise Volume 9 Hypersensitivity: Springer Science & Business Media; 2013.
[36] Lee D-E, Koo H, Sun I-C, Ryu JH, Kim K, Kwon IC. Multifunctional nanoparticles for multimodal imaging and theragnosis. Chem. Soc. Rev. 2012;41:2656-72.
[37] Key J, Leary JF. Nanoparticles for multimodal in vivo imaging in nanomedicine. Int. J. Nanomedicine. 2014.
[38] Lee N, Yoo D, Ling D, Cho MH, Hyeon T, Cheon J. Iron Oxide Based Nanoparticles for Multimodal Imaging and Magnetoresponsive Therapy. Chem. Rev. 2015;115:10637-89.
[39] Zhao Z, Fan H, Zhou G, Bai H, Liang H, Wang R, et al. Activatable Fluorescence/MRI Bimodal Platform for Tumor Cell Imaging via MnO2 Nanosheet–Aptamer Nanoprobe. JACS. 2014;136:11220-3.
[40] Sowers MA, McCombs JR, Wang Y, Paletta JT, Morton SW, Dreaden EC, et al. Redox-responsive branched-bottlebrush polymers for in vivo MRI and fluorescence imaging. Nat. Commun. 2014;5.
[41] Brown G, Daniels I, Richardson C, Revell P, Peppercorn D, Bourne M. Techniques and trouble-shooting in high spatial resolution thin slice MRI for rectal cancer. Br. J. Radiol. 2014.

Figure 1. Synthesis and characterization of Ce6(Mn)@$CaCO_3$-PEG nanoparticles. (a) A scheme showing the synthesis and structure of Ce6(Mn)@$CaCO_3$-PEG nanoparticles. (b&c) SEM (b) and TEM (c) images of as-synthesized Ce6(Mn)@$CaCO_3$ nanoparticles. (d) Scanning TEM (STEM) images of Ce6(Mn)@$CaCO_3$ showing the calcium K edge (yellow), oxygen L edge (red) and manganese L edge (green). (e) UV-Vis-NIR spectra of free Ce6, Ce6(Mn)@$CaCO_3$ and Ce6(Mn)@$CaCO_3$-PEG solutions. (f) Dynamic light scattering (DLS) data of Ce6(Mn)@$CaCO_3$-PEG in the aqueous solution. (g) A photograph of Ce6(Mn)@$CaCO_3$-PEG nanoparticles in water, PBS and cell medium solutions after incubation for 24 h.

Figure 2. (a) Schematic illustration showing the pH-responsive decomposition of Ce6(Mn)@$CaCO_3$-PEG nanoparticles. (b) Representative TEM images of Ce6(Mn)@$CaCO_3$-PEG after being immersed in PBS buffers with different pH values (5.5, 7.4 and 6.5) for different periods of time. Scale bar = 200 nm. (c) Time-dependent DLS-measured size changes of Ce6(Mn)@$CaCO_3$-PEG in PBS with the different pH values (5.5, 6.5 and 7.4).

Figure 3. pH-triggered MR enhancement and MR-imaging monitored drug release. (a) Time-dependent Ce6(Mn) release from Ce6(Mn)@$CaCO_3$-PEG in PBS with the different pH values. (b) T1-weighted MR images of Ce6(Mn)@$CaCO_3$-PEG with various concentrations taken 4 h after incubation in PBS at three different pH values. (c) T1 relaxivities of Ce6(Mn)@$CaCO_3$-PEG at different pH values corresponding to figure (b). (d) UV-Vis-NIR spectra of DOX loaded Ce6(Mn)@$CaCO_3$-PEG with different feeding concentration of DOX. (e) Time-dependent T1-MR images of Ce6(Mn)@$CaCO_3$-PEG(DOX) after incubation in PBS with different pH values. (f) Correlation between the percentage of released DOX and enhanced T1-MR signals over time at three pH values. Error bars were based on at least triplicated measurements. It is feasible to monitor drug release from those nanoparticles by MR imaging. (g) T1-weighted MR image of tumor-bearing mouse before and after administration of Ce6(Mn)@$CaCO_3$-PEG within tumor and normal subcutaneous tissue. (h) Plot of MR signal intensity enhancement (Tumor / muscle) versus time after injection of Ce6(Mn)@$CaCO_3$-PEG. Error bars were based on at least triplicated measurements.

Figure 4. In vitro cell culture experiments. (a) Confocal fluorescence images of 4T1 cells incubated with Ce6(Mn)@$CaCO_3$-PEG for 4 h. (b) Relative viabilities of 4T1 cells after being incubated with free DOX or Ce6(Mn)@$CaCO_3$-PEG(DOX) at various DOX concentrations for 24 h in dark. (c) Relative viabilities of 4T1 cells after incubation with different concentrations of Ce6 and Ce6(Mn)@$CaCO_3$-PEG 24 h post 660-nm light irradiation at 5 mW/cm^2 for 0.5h (+L). (d) Relative viabilities of 4T1 cells after being treated with Ce6(Mn)@$CaCO_3$-PEG, Ce6(Mn)@$CaCO_3$-PEG + Light irradiation (+L), Ce6(Mn)@$CaCO_3$-PEG(DOX), and Ce6(Mn)@$CaCO_3$-PEG(DOX) + L. P values in figure d was calculated by Tukey's post-test (***$p<0.001$, **$p < 0.01$, or *$p < 0.05$).

Figure 5. In vivo imaging. (a) Time-dependent in vivo fluorescence imaging of mice post i.v. injection of $CaCO_3$@Ce6(Mn)-PEG(DOX) nanoparticles by recording Ce6 fluorescence. (b) Ex vivo fluorescence imaging of the tumor and other organs taken at 24 h post-injection. (c) Distribution of $CaCO_3$@Ce6(Mn)-PEG(DOX) in 4T1 tumor-bearing mice determined by fluorescence of Ce6 (n = 3). (d) T1-weighted MR images of the same mouse taken before injection (left) and 24 h post i.v. injection (right) with $CaCO_3$@Ce6(Mn)-PEG(DOX). (e) Region-of-interest analysis of T1-weighted MR signals intensity in the tumor before injection and 24 h post i.v.

injection with nanoparticles. (f) T1-weighted MR image of a tumor-bearing mouse before and after local injection of Ce6(Mn)@$CaCO_3$-PEG within tumor and normal subcutaneous tissue. (g) Plot of MR signal intensity enhancement (Tumor / muscle) versus time after injection of Ce6(Mn)@$CaCO_3$-PEG. Error bars were based on at least triplicated measurements.

Figure 6. In vivo combination therapy. (a) Tumor growth curves of different groups of mice after various treatments (5 mice for each group). (b) The body weight variation of 4T1 tumor-bearing mice during different treatments. (c) Average weights of tumors collected from mice at day 12 after various treatments indicated. (d) A photo of the tumors collected from all different groups of mice at the end of treatments. (e) Micrographs of H&E (upper) and TUNEL (bottom) stained slices of tumors collected from mice one day after various treatments were given. Note: groups 1-5 refer to PBS (1), free Ce6 and DOX + L (2), Ce6(Mn)@$CaCO_3$-PEG(DOX) (3), Ce6(Mn)@$CaCO_3$-PEG + L (4) and Ce6(Mn)@$CaCO_3$-PEG(DOX) + L (5). P values in (a&c) were calculated by Tukey's post-test (***$p<0.001$, **$p < 0.01$, or *$p < 0.05$).

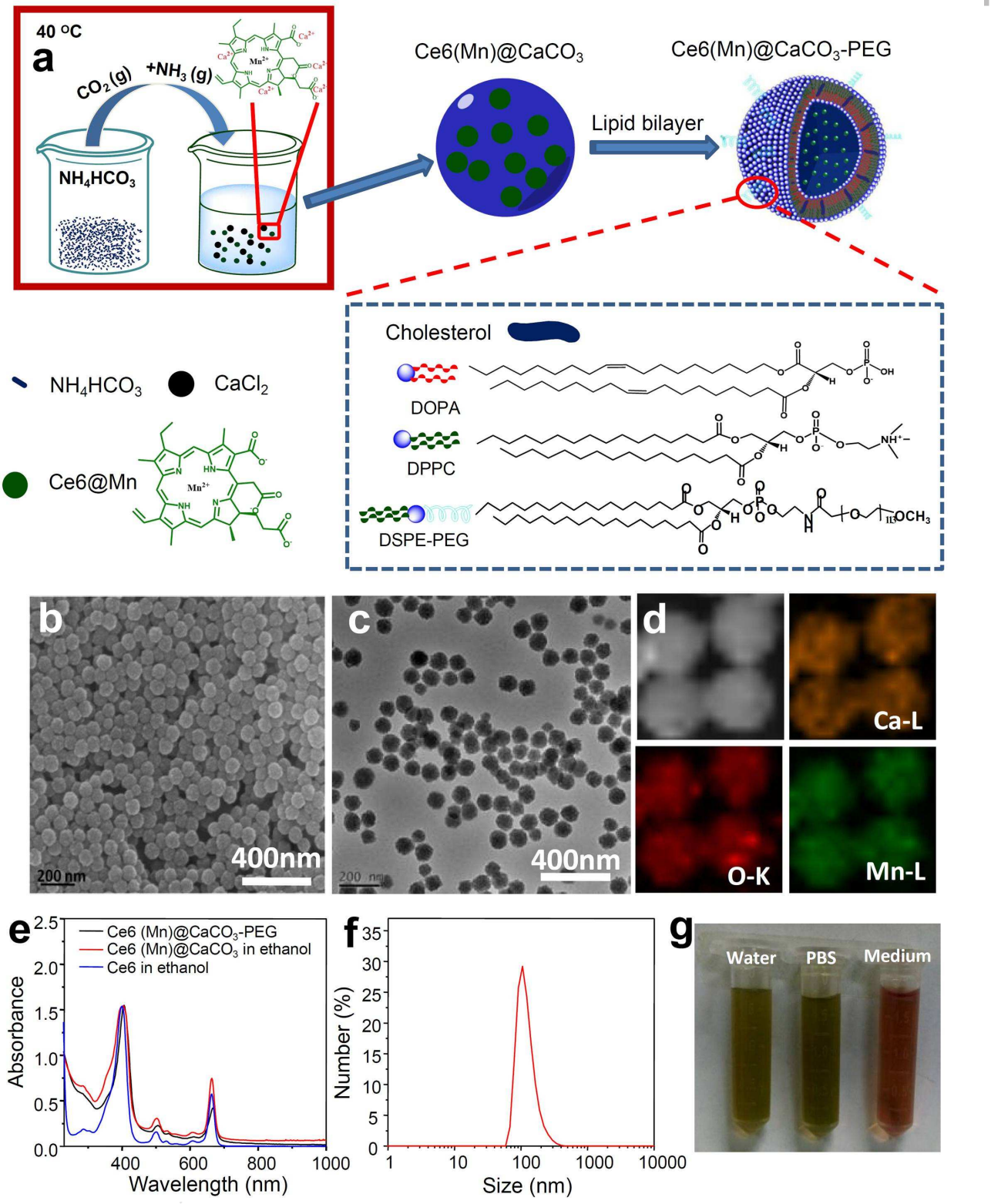

Figure 1. Synthesis and characterization of Ce6(Mn)@$CaCO_3$-PEG nanoparticles. (a) A scheme showing the synthesis and structure of Ce6(Mn)@$CaCO_3$-PEG nanoparticles. (b&c) SEM (b) and TEM (c) images of as-synthesized Ce6(Mn)@$CaCO_3$ nanoparticles. (d) Scanning TEM (STEM) images of Ce6(Mn)@$CaCO_3$ showing the calcium K edge (yellow), oxygen L edge (red) and manganese L edge (green). (e) UV-Vis-NIR spectra of free Ce6, Ce6(Mn)@$CaCO_3$ and Ce6(Mn)@$CaCO_3$-PEG solutions. (f) Dynamic light scattering (DLS) data of Ce6(Mn)@$CaCO_3$-PEG in the aqueous solution. (g) A photograph of Ce6(Mn)@$CaCO_3$-PEG nanoparticles in water, PBS and cell medium solutions after incubation for 24 h.

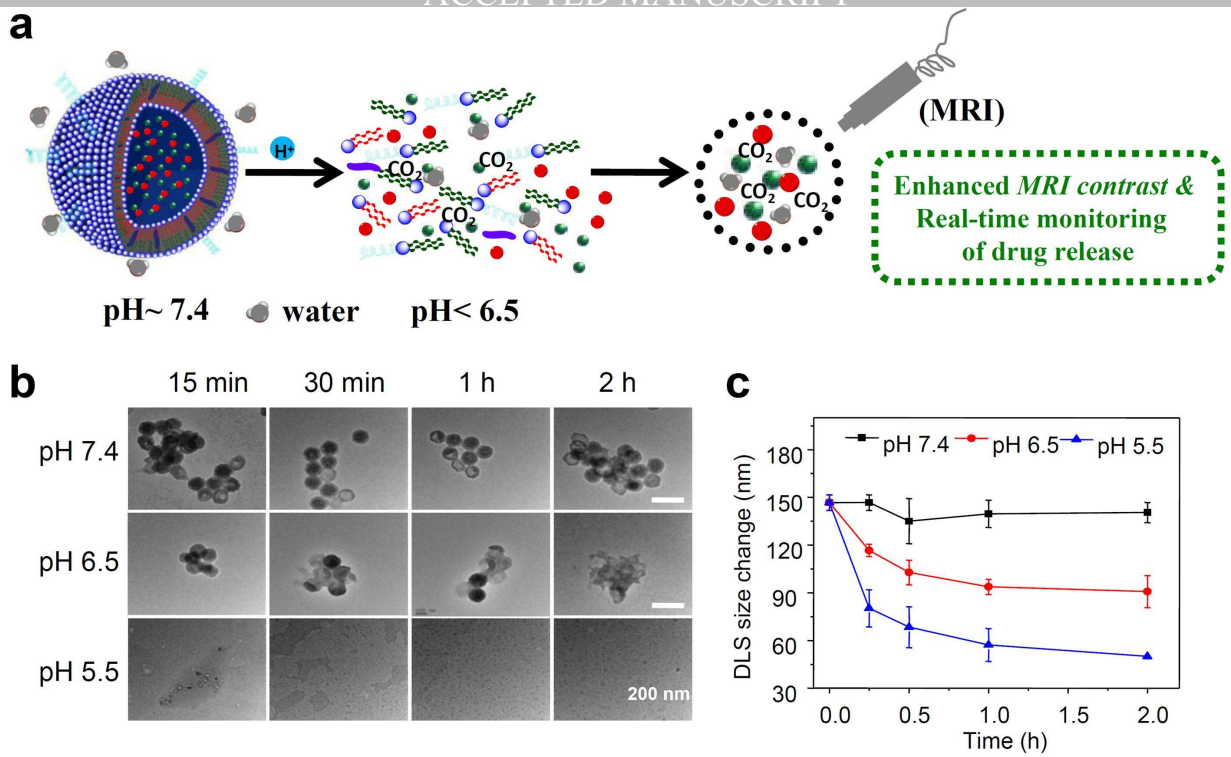

Figure 2. (a) Schematic illustration showing the pH-responsive decomposition of Ce6(Mn)@$CaCO_3$-PEG nanoparticles. (b) Representative TEM images of Ce6(Mn)@$CaCO_3$-PEG after being immersed in PBS buffers with different pH values (5.5, 7.4 and 6.5) for different periods of time. Scale bar = 200 nm. (c) Time-dependent DLS-measured size changes of Ce6(Mn)@$CaCO_3$-PEG in PBS with the different pH values (5.5, 6.5 and 7.4).

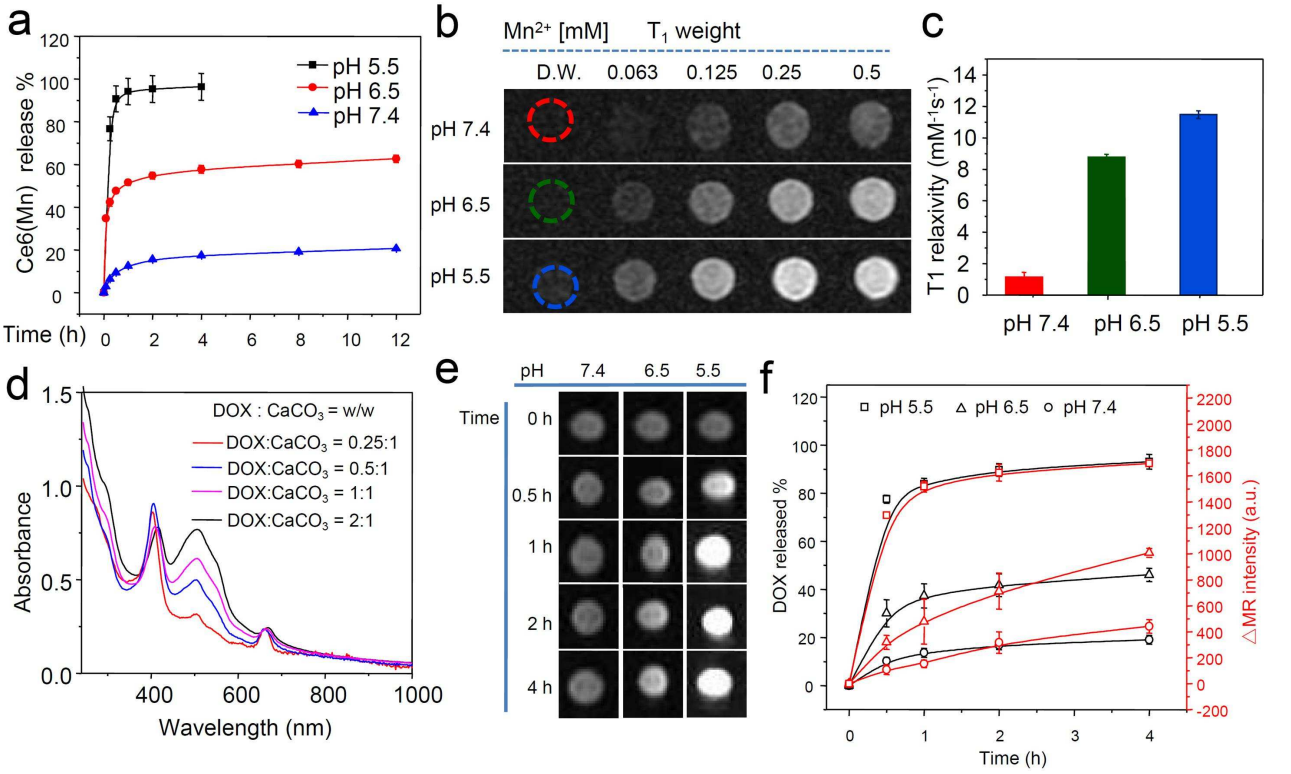

Figure 3. pH-triggered MR enhancement and MR-imaging monitored drug release. (a) Time-dependent Ce6(Mn) release from Ce6(Mn)@$CaCO_3$-PEG in PBS with the different pH values. (b) T1-weighted MR images of Ce6(Mn)@$CaCO_3$-PEG with various concentrations taken 4 h after incubation in PBS at three different pH values. (c) T1 relaxivities of Ce6(Mn)@$CaCO_3$-PEG at different pH values corresponding to figure (b). (d) UV-Vis-NIR spectra of DOX loaded Ce6(Mn)@$CaCO_3$-PEG with different feeding concentration of DOX. (e) Time-dependent T1-MR images of Ce6(Mn)@$CaCO_3$-PEG(DOX) after incubation in PBS with different pH values. (f) Correlation between the percentage of released DOX and enhanced T1-MR signals over time at three pH values. Error bars were based on at least triplicated measurements. It is feasible to monitor drug release from those nanoparticles by MR imaging.

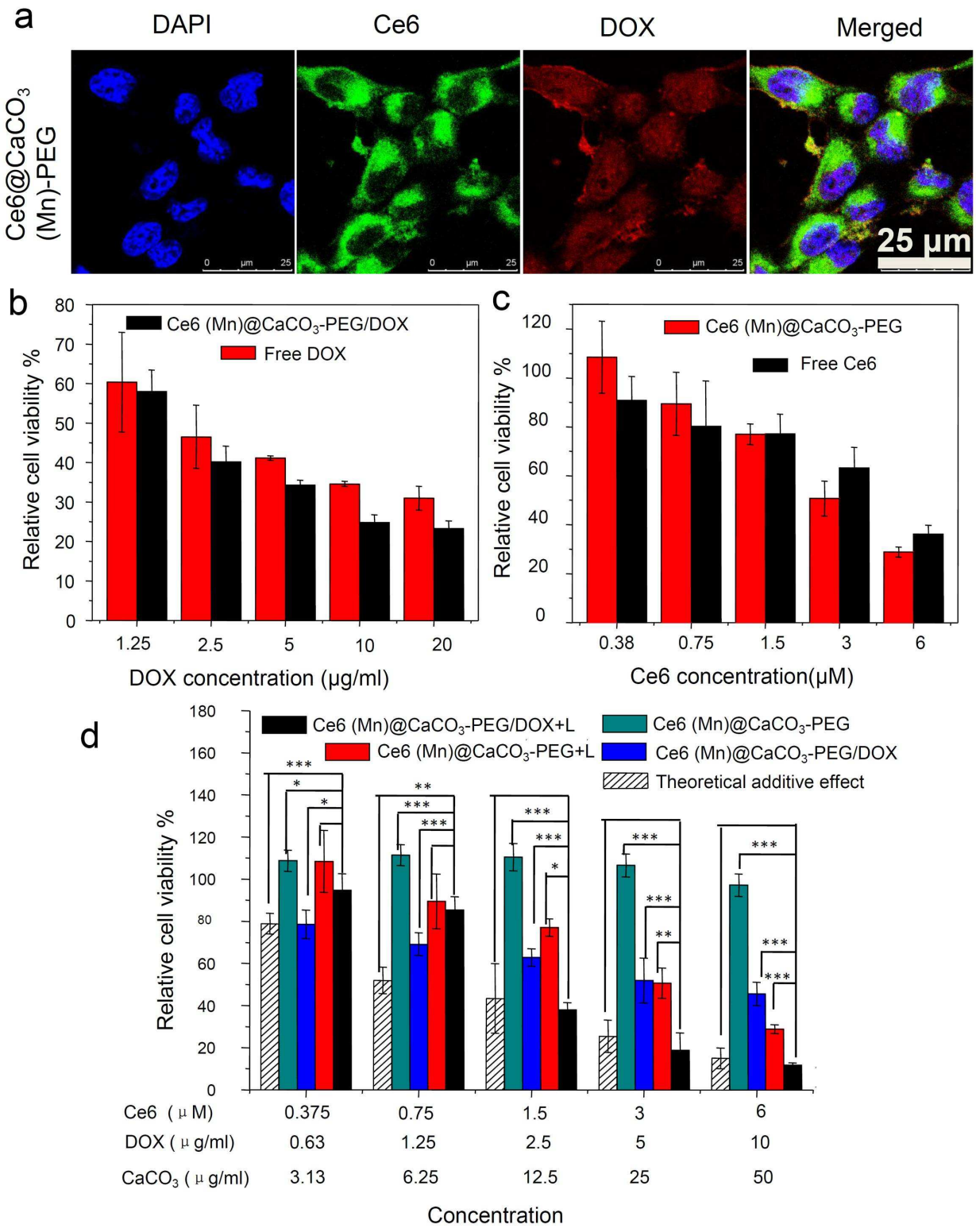

Figure 4. In vitro cell culture experiments. (a) Confocal fluorescence images of 4T1 cells incubated with Ce6(Mn)@$CaCO_3$-PEG for 4 h. (b) Relative viabilities of 4T1 cells after being incubated with free DOX or Ce6(Mn)@$CaCO_3$-PEG(DOX) at various DOX concentrations for 24 h in dark. (c) Relative viabilities of 4T1 cells after incubation with different concentrations of Ce6 and Ce6(Mn)@$CaCO_3$-PEG 24 h post 660-nm light irradiation (5mW/cm^2, 0.5h). (d) Relative viabilities of 4T1 cells after being treated with Ce6(Mn)@$CaCO_3$-PEG, Ce6(Mn)@$CaCO_3$-PEG + Light

irradiation (+L), Ce6(Mn)@$CaCO_3$-PEG(DOX), and Ce6(Mn)@$CaCO_3$-PEG(DOX) + L. P values in figure d was calculated by Tukey's post-test (***$p<0.001$, **$p < 0.01$, or *$p < 0.05$).

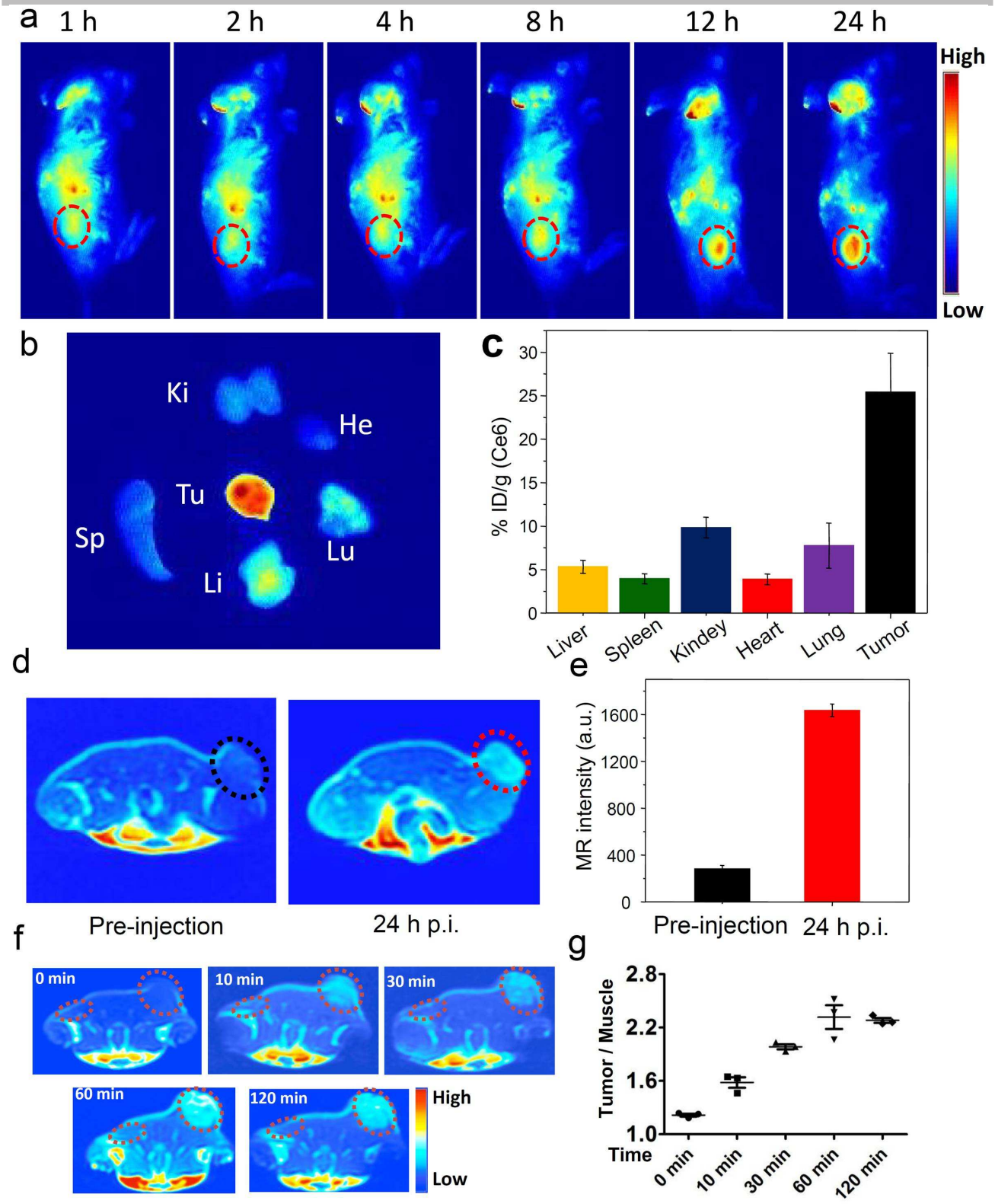

Figure 5. In vivo dual-modal imaging of 4T1 tumor-bearing mice post i.v. injection of $CaCO_3$@Ce6(Mn)-PEG(DOX) nanoparticles. (a) Time-dependent in vivo fluorescence imaging of mice post i.v. injection of those nanoparticles by recording Ce6 fluorescence. (b) Ex vivo fluorescence imaging of the tumor and other organs collected taken at 24 h post-injection. (c) Distribution of $CaCO_3$@Ce6(Mn)-PEG(DOX) in 4T1 tumor-bearing mice determined by fluorescence of Ce6 in tumors and normal tissues (n = 3). (d) T1-weighted MR images of the same mouse taken before injection (left) and 24 h post i.v. injection (right) with

$CaCO_3$@Ce6(Mn)-PEG(DOX). (e) Region-of-interest analysis of T1-weighted MR signals intensity in the tumor before injection and 24 h post i.v. injection with nanoparticles. (f) T1-weighted MR image of tumor-bearing mouse before and after administration of Ce6(Mn)@$CaCO_3$-PEG within tumor and normal subcutaneous tissue. (g) Plot of MR signal intensity enhancement (Tumor / muscle) versus time after injection of Ce6(Mn)@$CaCO_3$-PEG. Error bars were based on at least triplicated measurements.

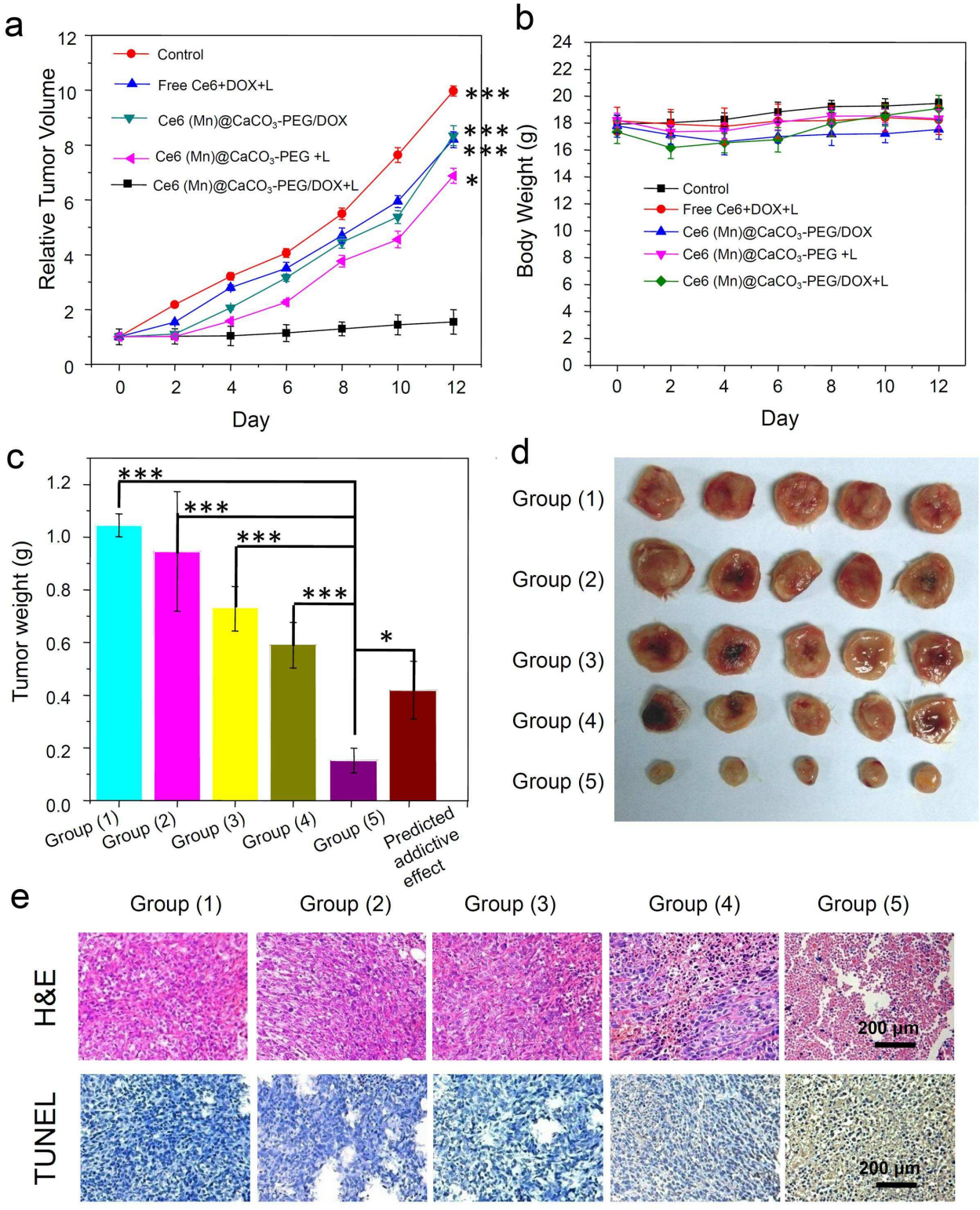

Figure 6. In vivo combination therapy. (a) Tumor growth curves of different groups of mice after various treatments (5 mice for each group). (b) The body weight variation of 4T1 tumor-bearing mice during treatment. (c) Average weights of tumors collected from mice at day 12 after various treatments indicated. (d) A photo of the tumors collected from all different groups of mice at the end of treatments. (e) Histological analysis of tumor after various treatments indicated. TUNEL (upper) and H&E (bottom) stained slices of tumors were collected from mice one day after various treatments indicated. Note: group (1), (2), (3), (4) and (5) were used to represent PBS (1), free Ce6 and DOX + L (2), Ce6(Mn)@$CaCO_3$-PEG(DOX) (3), Ce6(Mn)@$CaCO_3$-PEG + L (4) and

Ce6(Mn)@$CaCO_3$-PEG(DOX) + L (5). P values in (a& c) were calculated by Tukey's post-test (***p<0.001, **p < 0.01, or *p < 0.05).